

Sensitivity-Informed Augmentation for Robust Segmentation

Laura Zheng
lyzheng@umd.edu
Department of Computer Science,
University of Maryland
College Park, Maryland, USA

Wenjie Wei
wwei@terpmail.umd.edu
Department of Computer Science,
University of Maryland
College Park, Maryland, USA

Tony Wu
tonywu@terpmail.umd.edu
Department of Computer Science,
University of Maryland
College Park, Maryland, USA

Jacob Clements
clem012@umd.edu
Department of Computer Science,
University of Maryland
College Park, Maryland, USA

Shreelekha Revankar
revankar@cornell.edu
Department of Computer Science,
Cornell University
Ithaca, New York, USA

Andre Harrison
andre.v.harrison2.civ@army.mil
DEVCOM Army Research Laboratory
Adelphi, Maryland, USA

Yu Shen
yushen@adobe.com
Adobe Research
San Jose, California, USA

Ming C. Lin
lin@umd.edu
Department of Computer Science,
University of Maryland
College Park, Maryland, USA

ABSTRACT

Segmentation is an integral module in many visual computing applications such as virtual try-on, medical imaging, autonomous driving, and agricultural automation. These applications often involve either widespread consumer use or highly variable environments, both of which can degrade the quality of visual sensor data, whether from a common mobile phone or an expensive satellite imaging camera. In addition to external noises like user difference or weather conditions, internal noises such as variations in camera quality or lens distortion can affect the performance of segmentation models during both development and deployment. In this work, we present an efficient, adaptable, and gradient-free method to enhance the robustness of learning-based segmentation models across training. First, we introduce a novel *adaptive sensitivity analysis* (ASA) using Kernel Inception Distance (KID) on basis perturbations to benchmark perturbation sensitivity of pre-trained segmentation models. Then, we model the sensitivity curve using the adaptive SA and sample perturbation hyperparameter values accordingly. Finally, we conduct adversarial training with the selected perturbation values and dynamically re-evaluate robustness during online training. Our method, implemented end-to-end with minimal fine-tuning required, consistently outperforms state-of-the-art data augmentation techniques for segmentation. It shows significant improvement in both clean data evaluation and real-world adverse scenario evaluation across various segmentation datasets used in visual computing and computer graphics applications.

Permission to make digital or hard copies of all or part of this work for personal or classroom use is granted without fee provided that copies are not made or distributed for profit or commercial advantage and that copies bear this notice and the full citation on the first page. Copyrights for components of this work owned by others than the author(s) must be honored. Abstracting with credit is permitted. To copy otherwise, or republish, to post on servers or to redistribute to lists, requires prior specific permission and/or a fee. Request permissions from permissions@acm.org.
Preprint, June 03, 2024, USA

© 2024 Copyright held by the owner/author(s). Publication rights licensed to ACM.
ACM ISBN 978-x-xxxx-xxxx-x/YY/MM
<https://doi.org/10.1145/nmnnnnn.nmnnnnn>

2024-06-05 00:37. Page 1 of 1–16.

KEYWORDS

Segmentation, Robustness, Deep Learning, Sensitivity Analysis

ACM Reference Format:

Laura Zheng, Wenjie Wei, Tony Wu, Jacob Clements, Shreelekha Revankar, Andre Harrison, Yu Shen, and Ming C. Lin. 2024. Sensitivity-Informed Augmentation for Robust Segmentation. In *Proceedings of (Preprint)*. ACM, New York, NY, USA, 16 pages. <https://doi.org/10.1145/nmnnnnn.nmnnnnn>

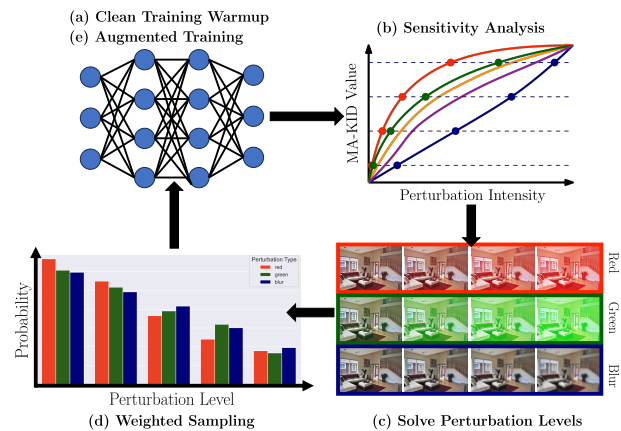


Figure 1: Overview of our method. We present a gradient-free method for augmenting semantic segmentation models based on adaptive sensitivity analysis. We conduct sensitivity analysis using our Fast Sensitivity Analysis algorithm after a warmup period on clean data, then solve for L discrete perturbation levels per perturbation type at which the model is sensitive to. Finally, we augment training by sampling from the computed perturbation levels. Sampling weights are determined based off model performance on sensitive levels, where worse-performing levels are given higher probability of being sampled.

1 INTRODUCTION

In most applications, segmentation models face unpredictable and uncontrollable natural variables. For example, phone applications that use segmentation in reconstruction pipelines can experience various noises from their user base, depending on factors like environment lighting, camera quality, and angle preferences. Similarly, outdoor robots or autonomous vehicles may encounter a range of adverse weather conditions that are challenging to simulate accurately. Even when natural variables are predictable and controllable, simulating them within the same domain as the data remains extremely difficult. Segmentation models in medical imaging require the subject and camera to be very still during capture to avoid blurred input data. Home robots' camera sensors may collect debris or be obstructed by fingerprints from user handling. While poor-quality examples can sometimes be discarded and re-captured, such solutions are costly or impractical, especially in large-scale, ubiquitous use cases, with limited resources, and during real-time inference (e.g., failure in a navigating robot).

Incorporating natural corruptions into model training is challenging because these corruptions are an inherent part of the data domain and are combinatorially difficult to account for. Unlike classical data augmentations, where the space of possible cut and crop dimensions can be thoroughly sampled, natural corruptions are unbounded and thus nontrivial to sample.

Robustifying neural networks against natural corruptions is often addressed through data augmentation techniques. However, popular augmentation techniques typically focus on single-image classification or regression tasks. Recent work [Kamann and Rother 2020] has shown that for semantic segmentation tasks, robustness directly correlates with performance on clean data. Despite this, baseline results for corruptions on segmentation models still show significant performance degradation, and popular data augmentation techniques offer less pronounced improvements for semantic segmentation. Our focus is on addressing robustification against natural corruptions in semantic segmentation.

Previous methods for improving robustness often fall short in at least one of three areas: (1) *computational scalability*, in that the method scales reasonably to larger datasets and diverse classes relative to hardware resources, (2) *generalization to natural corruptions*, where the model is not only robust to clean evaluation data, but also corrupted evaluation data, or (3) *reliance on differentiable corruptions*, where synthetically applied corruptions are well-defined and differentiable transformation functions. To the best of our knowledge, no existing works address all three issues comprehensively.

In this paper, we introduce a scalable, end-to-end, and generalized learning approach for robustifying segmentation models against natural corruptions, including those not explicitly involved during training. While popular data augmentation techniques generally scale well, many require an external model trained offline to guide augmentation or rely on random augmentation. Methods using sensitivity analysis (SA) provides improved performance over traditional augmentation techniques, but modeling the sensitivity of a model with non-differentiable augmentations is computationally expensive [Shen et al. 2021]. Our method uses the best of both worlds, offering a data augmentation technique that is scalable and

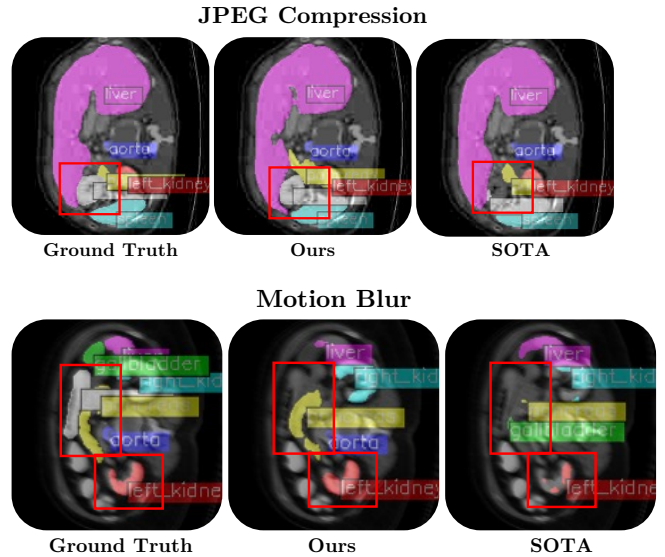


Figure 2: Qualitative segmentation comparison between our method and SOTA on abdomen CT organ classification in the presence of JPEG Compression and Motion Blur. JPEG Compression and Motion blur are two common types of noises present in medical datasets. On the top example, a small amount of JPEG compression completely masks the SOTA model’s capability to detect the stomach (white). On the bottom, we show that motion blur on the input image causes issues in identifying the pancreas (yellow) and the left kidney (red). Ours outperform SOTA in both.

efficient like random augmentation techniques, but also keeps the sophistication provided by sensitivity-based techniques.

We achieve this by conducting a *lightweight, online sensitivity analysis* to identify the photometric perturbations, shown to be effective as "basis perturbations" [Shen et al. 2021], to which the model is most sensitive. However, in contrast to [Shen et al. 2021], we dynamically sample these perturbations and weight them based on the model’s sensitivity at different intensity levels. As a result, our method achieves up to a 34.8% improvement in generalization performance to synthetically perturbed data.

Our contributions are summarized as follows:

- (1) An efficient *adaptive* sensitivity analysis method for *online model evaluation* that utilizes approximate monotonicity of model sensitivity for speedup;
- (2) A comprehensive framework that leverages sensitivity analysis results to systematically improve robustness of learning-based segmentation models;
- (3) Evaluation and analysis of our method on *unseen* synthetically perturbed samples, *naturally corrupted* samples, and ablated contributing factors to robustification.

2 RELATED WORKS

Robustification Against Natural Corruptions. The effect of natural corruptions on deep learning tasks is a well-explored problem, especially in image classification. Currently, image classification

has a robust suite of benchmarks, including evaluation on both synthetic and natural corruptions [Dong et al. 2020; Hendrycks et al. 2020; Yi et al. 2021]. Many works study correlations between image corruptions and various factors [Hendrycks and Gimpel 2017; Mintun et al. 2021]. Several approaches target model architecture [Saikia et al. 2021; Schneider et al. 2020]. Other approaches achieve robustness to natural corruptions via the data pipeline. Data augmentations are a popular method for increasing out-of-distribution robustness and many have now become standard practice [Geirhos et al. 2019; Rusak et al. 2020]. Hendrycks et al. highlight that existing methods for generalization may not be consistently effective, emphasizing the need for robustness through addressing multiple distribution shifts [Hendrycks et al. 2021].

In our work, we focus on studying and improving robustness in the context of semantic segmentation models against natural corruptions using insights from previous work. Firstly, we consider from [Kamann and Rother 2020] (who benchmarked robustness of segmentation models) that robustness in segmentation models differ from the traditional image classification setting used in most robustness approaches, in that the clean accuracy of segmentation models scale directly with robustness. Secondly, we also consider from [Mintun et al. 2021] that augmentations visually correlate with the “type” of robustness it provides. Among findings from other works, we distinguish that our work focuses on improving natural corruption robustness in a segmentation, a common task with unique properties.

Data Augmentation Techniques. Data augmentation methods generate variants of the original training data to improve model generalization capabilities. These variants do not change the inherent semantic meaning of the image, and transformed images are typically still recognizable by humans.

Within data augmentation methods, CutMix and AugMix are the most well-known and widely used [Hendrycks et al. 2020; Yun et al. 2019]. Other data augmentation methods have utilized machine learning techniques to select more optimal augmentations [Cubuk et al. 2019; Olsson et al. 2021; Zheng et al. 2022], while other works have explored data augmentation for domain-specific tasks [Zhang et al. 2023; Zhao et al. 2019]. For example, [Zhao et al. 2019] explores learned data augmentation for biomedical segmentation tasks via labeling of synthesized samples with a single brain atlas. [Zhang et al. 2023] explores data augmentation via combining multiple brain scan samples. These methods are specific to biomedical imaging in addition to addressing overall generalization capabilities, rather than robustness to natural corruptions.

3 BACKGROUND: BASIS AUGMENTATIONS

Previous work in robustification showed that learning with a set of “basis perturbations” (BP) significantly improved zero-shot evaluation against unseen corruptions [Shen et al. 2021] for image classification and regression tasks, such as vehicle steering prediction. The intuition behind basis perturbations is that the composition of such perturbations spans a much larger space of perturbations than may be observed in natural corruptions; observed zero-shot performance boosts on unseen corruptions subsequently might be attributed to learning a model which is robust to basis perturbations. In our method, we extend this concept and introduce a

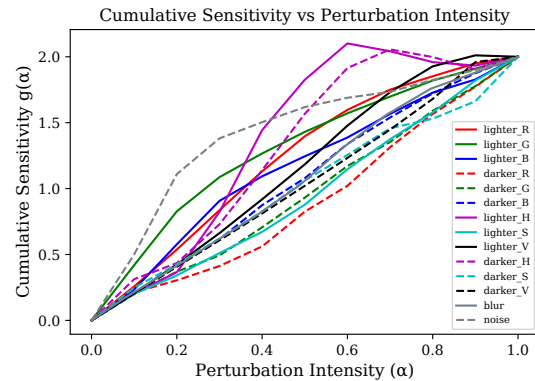


Figure 3: Cumulative Sensitivity Curve g for photometric augmentations on baseline Cityscapes Model. We show the computed cumulative sensitivity curve described by Equation 8 for a baseline Cityscapes model trained on PSPNet architecture. We periodically compute this curve during training and augment with α values solved with Equation 9.

more generalized and larger set of basis perturbations in sensitivity analysis to determine the most productive augmentation during training.

Let $D = \{Positive, Negative\}$ describe the set of augmentations applied in either a positive (lighter) direction or negative (darker) to either one channel of an image or a parameter of an affine transformation applied to an image.

Let $P = \{R, G, B, H, S, V\}$ describe the set of channels in RGB and HSV color spaces which may be perturbed; in other words, these augmentations are *photometric*.

Then, let $G = \{ShearX, ShearY, TranslateX, TranslateY, Rotate\}$ denote affine, or *geometric*, transformations which are parameterized by a magnitude value.

Finally, let $Z = \{Noise, Blur\}$ be the set of augmentations not applied along channel dimensions. Specifically, we use Gaussian Noise and Gaussian Blur.

Thus, the set of all basis augmentations A_B used in robustification is $A_B = \{D \times P + G + Z\}$.

To compute lighter or darker channel augmentations of RGB or HSV channels, we use linear scaling. Let the range of a channel be $[v_{min}, v_{max}]$. For lighter channel augmentations, we transform the channel values v_C by an intensity factor α like so:

$$v'_C = \alpha v_{max} + (1 - \alpha) \cdot v_C$$

Likewise, for darker channel augmentations, the transformation can be described like so:

$$v'_C = \alpha v_{min} + (1 - \alpha) \cdot v_C$$

The default values are $v_{min} = 0$ and $v_{max} = 255$. For H channel augmentations, we set the maximum channel values to be 180. For V channel augmentations, we set the minimum channel values to be 10 to exclude completely dark images.

Affine transformations can be represented as a 3×3 matrix, which, when multiplied with a 2-dimensional image, produces a

geometrically distorted version of that image. Affine transformation matrices are typically structured in the form:

$$M = \begin{bmatrix} 1 & Shear_X & T_x \\ Shear_Y & 1 & T_y \\ 0 & 0 & 1 \end{bmatrix}$$

for shear and translation transformations. For rotations where the center of the image is fixed as the origin point $(0, 0)$, the transformation matrix is defined as:

$$M_{rot} = \begin{bmatrix} \cos\theta & -\sin\theta & 0 \\ \sin\theta & \cos\theta & 0 \\ 0 & 0 & 1 \end{bmatrix}$$

To account for padded values in images after affine transformations, we zoom in images to the largest rectangle such that padded pixels are cropped out.

All augmentations are parameterized by a magnitude value ranging from 0 to 1. A magnitude value of 1 corresponds to the most severe augmentation value. More details on exact parameter value ranges can be found in the appendix. Conversely, a magnitude value of 0 produces no changes to the original image, and can be considered an identity function. We account for the symmetry of these augmentation transformations by considering both positive values and negative values separate augmentations. The fast adaptive sensitivity analysis algorithm introduced in the next section relies on the property that increasing magnitude corresponds to increasing “distance” between images. Thus, augmentations cannot simply span the value ranges -1 to 1, and we separate them instead to different augmentations (positive and negative).

We apply these augmentations on-the-fly in online learning rather than generating samples offline. Doing so greatly reduces the offline storage requirement by one order of magnitude. Suppose L intensity levels are sampled for each basis augmentation. Then, offline generation of perturbed data requires up to $L \times 2 \times (|P| + |G|) + 2 = 24L$ additional copies of the original clean dataset. *With online generation, we avoid offline dataset generation entirely and only need the original clean dataset to be stored, similar to standard vanilla learning.*

4 METHODOLOGY

4.1 Sensitivity Analysis

Sensitivity analysis examines how uncertainty in the inputs (independent variables) affects the outputs (dependent variables) of a system. We systematically estimate the sensitivity analysis curve to measure how uncertainties (augmentations) in image inputs will influence model performance.

Kernel Inception Distance. Sensitivity analysis requires a quantifiable and standardized metric to represent the extent of input data changes. We use a measure of distance between a clean dataset and its perturbed version to represent change in independent variable. While Frechet Inception Distance (FID) is a popular choice for this, especially in generative modeling, Kernel Inception Distance (KID) offers advantages by reducing bias related to sample size [Bińkowski et al. 2018]. Unlike FID, which assumes a parametric form for activation distributions, KID uses squared Maximum Mean Discrepancy (MMD) with a polynomial kernel to

measure the distance between features of clean and perturbed data when passed through an Inception model. KID does not require fitting a quadratic covariance matrix, thus converging faster even for smaller sample sizes. We use KID in sensitivity analysis to quantify the extent of augmentation.

Sensitivity Analysis Objective. We measure the output model performance with the mean Intersection-over-Union (IoU) metric, denoted as MA , due to its resistance to class imbalances compared to pixel accuracy metrics. For generalization purposes, any metric where higher numbers indicate higher model performance can be substituted in sensitivity analysis.

Suppose the training dataset $X = \{x_1, x_2, \dots, x_N\}$ of size N consists of original, unperturbed (clean) samples x_i . Then, the perturbed training dataset $T_\alpha(X) = \{T_\alpha(x_1), T_\alpha(x_2), \dots, T_\alpha(x_N)\}$ is produced by applying an augmentation transformation T_α to the original samples, with the intensity or level of augmentation parameterized by α . We sample L levels of increasing intensity values α , so that the set of augmentation functions used for augmentation in total for one augmentation class is $\{T_{\alpha_1}, \dots, T_{\alpha_L}\}$, where $\alpha_1 < \alpha_2 < \dots < \alpha_L$.

Given the MA and KID values for L augmentation levels of increasing intensity, we define the augmentation performance curve parameterized by X and T_α as

$$KID(X, \alpha) = MMD(f_0(X), f_0(T_\alpha(X)))^2 \quad (1)$$

$$MA(X, \alpha) = mIoU(Y, f(T_\alpha(X))) \quad (2)$$

where Y is the ground truth annotation, f is the function that describes a neural network, f_0 is the feature extractor of f , and MMD is Maximum Mean Discrepancy. In general, KID increases as the intensity of the augmentation α increases. That is, $KID(X, T_0) < KID(X, T_1) < \dots < KID(X, T_L)$.

In future descriptions, we truncate $KID(X, \alpha)$ and $MA(X, \alpha)$ to $KID(\alpha)$ and $MA(\alpha)$ respectively, since data input is constant.

Following this, we define sensitivity as the first-order derivative of this curve.

$$sensitivity = \frac{\partial MA}{\partial KID} \quad (3)$$

We want to minimize sensitivity, or the change in model accuracy when there are corruptions in the input data via the results of sensitivity analysis. To do so, we must find the augmentation levels to which the model is sensitive and use those levels in data augmentation.

We sample levels more densely in the ranges that have higher sensitivity. Intuitively, a model is sensitive to a particular augmentation level if the change in KID is small or the change in accuracy is large compared to that of the greatest level lower than the current sampled level. Specifically, to find these augmentation levels $\{\alpha_1, \dots, \alpha_{L-1}\} \in A$, we want to solve the objective Q for a fixed augmentation type T :

$$\Delta \widehat{MA}(\alpha', \alpha'') = \frac{MA(\alpha'') - MA(\alpha')}{MA(\alpha_o) - MA(\alpha_L)} \quad (4)$$

$$\Delta \widehat{KID}(\alpha', \alpha'') = \frac{KID(\alpha'') - KID(\alpha')}{KID(\alpha_L)} \quad (5)$$

$$Q = \underset{\{\alpha_1, \dots, \alpha_L\} \in A}{\operatorname{argmax}} \min_{1 \leq i \leq L} \Delta \widehat{MA}(\alpha_i, \alpha_{i-1}) - \Delta \widehat{KID}(\alpha_i, \alpha_{i-1}) + 2 \left(\frac{\alpha_i - \alpha_{i-1}}{\alpha_L} \right) \quad (6)$$

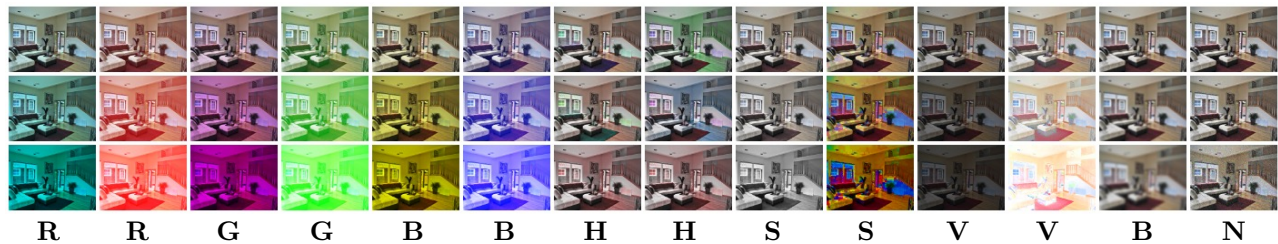


Figure 4: Visualization of each photometric augmentation transformation on a bedroom image. Up \uparrow indicates the “lighter”, positive direction and \downarrow indicates the “darker”, negative direction. “B” and “N” indicate blur and noise, respectively.



Figure 5: Visualization of various geometric augmentations applied to a sample image of a house. We use the following geometric transformations in our sensitivity analysis scheme, which are also analogous to the set of transformations used by other methods [Cubuk et al. 2019; Zheng et al. 2022]. Up arrows indicate augmentation in the *positive*, or left, direction, while down arrows indicate augmentation in the *negative*, or right, direction.

| Method | PSPNet [2017] | | | SegFormer [2021] | | |
|----------------|-----------------|-----------------|-----------------|------------------|-----------------|-----------------|
| | aAcc \uparrow | mAcc \uparrow | mIoU \uparrow | aAcc \uparrow | mAcc \uparrow | mIoU \uparrow |
| Baseline | 63.770 | 48.695 | 35.715 | 86.825 | 57.280 | 48.365 |
| Augmix | 94.770 | 74.400 | 66.740 | 95.520 | 81.430 | 73.390 |
| AutoAugment | 95.130 | 77.210 | 69.630 | 95.550 | 81.390 | 73.820 |
| RandAugment | 83.480 | 54.960 | 45.245 | 88.380 | 65.430 | 53.630 |
| TrivialAugment | 84.815 | 55.155 | 45.680 | 88.070 | 64.210 | 53.770 |
| SOTA | 94.910 | 77.270 | 69.860 | 95.850 | 83.980 | 76.300 |
| Ours | 95.100 | 79.320 | 71.840 | 95.880 | 84.070 | 76.330 |

Table 1: Comparison of performance metrics across different augmentation methods on Cityscapes. We evaluated our sensitivity-informed augmentation method against popular benchmarks on PSPNet and SegFormer. The baseline represents training with simple augmentations. Our method achieves comparable results to other methods which require chained, more computationally expensive augmentations or external augmentation models in terms of generalization to real-world scenarios.

where α_0 is the augmentation level of the original unperturbed dataset and α_L is the maximum value α can take on.

Fast Sensitivity Analysis. To solve for Q , one naive approach is to sample various augmentation values, then approximate the

MA-KID curve from evaluated MA and KID values. Although using a sensitivity curve to make informed augmentations is intuitive, the main drawback to using a sensitivity curve during training is the additional computational cost in estimating the sensitivity analysis curve itself. Since the augmentation itself is not guaranteed to be a differentiable transformation in practice (e.g., weather effects), we cannot use a gradient-based method to solve for the sensitivity curve. To obtain a point on the gradient-free sensitivity curve, a data set must be evaluated using a forward pass of the trained model f , as well as a forward pass through a pre-trained Inception V3 network. Thus, modeling the full sensitivity curve accurately can be expensive and infeasible to compute during online training. Since our goal is to augment training with augmentations from the solution to Equation 6, we only need to model the curve accurately in specific regions of interest. To do so, we show the analytical solution of Q .

We first rewrite Equation 6:

$$Q \approx \operatorname{argmax}_{\{\alpha_1, \dots, \alpha_L\} \in A} \min_{1 \leq i \leq L} g(\alpha_i) - g(\alpha_{i-1}) \quad (7)$$

| Method | Weather // ACDC [2021] | | | Domain // IDD [2019] | | |
|-------------|------------------------|--------------|--------------|----------------------|--------------|--------------|
| | aAcc↑ | mIoU↑ | mAcc↑ | aAcc↑ | mIoU↑ | mAcc↑ |
| Baseline | 52.38 | 14.62 | 26.01 | 69.07 | 21.80 | 40.58 |
| AugMix | 60.32 | 22.15 | 36.41 | 79.48 | 29.75 | 50.90 |
| AutoAugment | 56.72 | 26.87 | 40.33 | 80.79 | 31.93 | 52.62 |
| TrivialAug | 64.37 | 25.97 | 41.84 | 83.39 | 33.72 | 53.17 |
| RandAug | 63.47 | 26.03 | 41.10 | 82.51 | 33.11 | 53.83 |
| SOTA | 67.84 | 25.83 | 41.65 | 78.98 | 32.49 | 53.63 |
| Ours | 69.33 | 26.34 | 43.79 | 80.49 | 33.83 | 56.48 |

Table 2: Evaluation results on Real World Driving Datasets. We conduct zero-shot evaluation of Cityscape models on both ACDC [2021] and IDD [2019] datasets, which represent adverse weather and domain transfer to India respectively. Our method achieves clear improvements compared to other methods which require chained, more computationally expensive augmentations or external augmentation models in terms of generalization to real world scenarios, with relative mIoU improvement up to an 80.2% on ACDC and up to 55.2% on IDD compared to the baseline.

where

$$g(\alpha) = \frac{MA(\alpha_0) - MA(\alpha)}{MA(\alpha_0) - MA(\alpha_L)} - \frac{KID(\alpha)}{KID(\alpha_L)} + 2 \left(\frac{\alpha}{\alpha_L} \right) \quad (8)$$

We note that

$$\sum_{i=1}^L (g(\alpha_i) - g(\alpha_{i-1})) = g(\alpha_L) - g(\alpha_0) = 2.$$

Since $\Delta \widehat{MA}$ and $\Delta \widehat{KID}$ increase approximately monotonically, we can approximate Q :

$$Q^* \approx \left\{ \alpha_i \in A \mid g(\alpha_i) = \frac{2i}{L}, i = 1, \dots, L \right\} \quad (9)$$

From this, the optimal augmentation values with high sensitivity lie at the values where their evaluated $g(\alpha)$ values are equidistant intervals between 0 and $g(\alpha_L)$. An example visualization of g can be found in Figure 3, where we compute the curve for a baseline Cityscapes PSPNet model. Since we do not have the analytical inverse function g^{-1} to solve for the optimal augmentation values, we instead model it via simulation, prioritizing sampling around the regions around the intervals described above. At a high level, our strategy for modeling g involves adaptively sampling α values near approximated regions of interest.

We take advantage of two things: (1) the modeled curve only needs to be accurate around the intervals we are interested in, and (2) the curve is approximately monotonically increasing as α approaches the maximum value. We iteratively estimate the curve described by at least 2 waypoints. First, since we already know the minimum and maximum value g takes on is 0 at $\alpha = 0$ and 2 at $\alpha = 1$, the curve is at first approximately described by the line between the minimum and maximum points. We use this initial line to find the regions of interest along the curve to sample from by solving for the set of α_i in Equation 9. Then, we evaluate g at the α_i with the highest uncertainty. The curve is updated again based on this new set of evaluated waypoints, where the curve is smoothly fitted with a Piecewise Cubic Hermite Interpolating Polynomial (PCHIP). We solve for the augmentation values again from Equation 9, and

repeat. Additionally, we also make use of the minimal sample size bias of KID and use only a subset of the validation set to evaluate g , further reducing the computational cost of sensitivity analysis. The full routine is described in Algorithm 1 in the Appendix.

Training with sampled augmentations. The previous section explains how L levels are computed for one particular augmentation type T . In training, we compute L levels for each basis augmentation described in Section 3. In total, there are 24 basis augmentations, counting positive and negative directions. Thus, the sensitivity analysis step will compute $24L$ levels on each run.

To augment training with $24L$ different augmentation functions, we compute a discrete probability density function (PDF) based on the accuracy, or performance, of the model at each augmentation level. Since previous work has shown that segmentation model robustness scales directly with clean model performance [Kamann and Rother 2020], as opposed to the inverse for single-image classification tasks, we aim to augment training with easier augmentations while still representing more severe augmentations. We construct the discrete PDF based on model accuracy on perturbed evaluation data, for each level, and for each augmentation type.

If we denote T_i as the i -th highest or most severe augmentation level of a particular augmentation type T , then the probability of sampling the particular augmentation is

$$p(T_i|T) = \frac{MA(X, T_i)^2}{\sum_{j=1}^L MA(X, T_j)^2} \quad (10)$$

$$p(T) = \frac{1}{25} \quad (11)$$

where the denominator in the second term comes from there being 24 basis augmentations plus equal representation of clean data.

During training, an input is augmented with one sampled augmentation from this PDF at a time. Furthermore, we couple our augmentations with random resizing and cropping, which are standard augmentations used in segmentation. In our experiments, we train baselines with random resizing and cropping as well in order to show the effects of our augmentation scheme. The full training scheme is illustrated in Figure 1.

5 RESULTS

Hardware. Each experiment is conducted on four NVIDIA RTX A4000 GPUs and 16 AMD Epyc 16-core processors. Sensitivity analysis experiments are conducted on one GPU and 4 processors.

Experiment Setup. All experiments are conducted on the Pyramid Scene Parsing Network (PSPNet) architecture, except for our results on the Segformer architecture in Table 1. In addition, we use the recommended hyperparameter configuration for each experiment and baseline in order to show best performance capabilities of each method out-of-the-box. For experiments on our method, we update the sensitivity analysis curve at four equal intervals during training and evaluate the model at eight equal intervals. Training for all methods ends when the evaluation performance converges (early stopping) or when training iterations reaches 160k. To account for possible performance differences depending on hardware, we also re-train baseline models with similar configurations in order to maintain fair comparison. Models trained on our method are minimally fine-tuned and trained entirely end-to-end, similarly to other

| Method | Fog | | | Rain | | | Night | | | Snow | | |
|--------------------|-----------------|-----------------|-----------------|-----------------|-----------------|-----------------|-----------------|-----------------|-----------------|-----------------|-----------------|-----------------|
| | aAcc \uparrow | mAcc \uparrow | mIoU \uparrow | aAcc \uparrow | mAcc \uparrow | mIoU \uparrow | aAcc \uparrow | mAcc \uparrow | mIoU \uparrow | aAcc \uparrow | mAcc \uparrow | mIoU \uparrow |
| Baseline | 67.55 | 22.87 | 36.14 | 67.99 | 21.18 | 34.29 | 22.64 | 4.07 | 13.23 | 52.28 | 14.41 | 26.94 |
| AugMix [2020] | 70.07 | 32.68 | 51.16 | 70.92 | 27.82 | 45.43 | 43.85 | 10.91 | 21.60 | 56.94 | 21.25 | 39.45 |
| AutoAugment [2019] | 60.59 | 35.30 | 54.62 | 55.47 | 28.96 | 48.54 | 55.14 | 15.45 | 26.13 | 55.72 | 27.19 | 43.49 |
| TrivialAug [2021] | 76.19 | 39.38 | 59.17 | 67.60 | 27.76 | 48.32 | 53.91 | 13.62 | 23.82 | 60.09 | 25.54 | 43.98 |
| RandAug [2020] | 75.21 | 38.80 | 58.72 | 66.57 | 29.09 | 49.23 | 54.44 | 13.96 | 25.77 | 57.95 | 24.46 | 42.49 |
| SOTA [2020] | 86.41 | 47.13 | 61.61 | 82.20 | 32.64 | 45.01 | 28.28 | 8.47 | 18.90 | 75.72 | 29.89 | 41.85 |
| Ours | 87.07 | 48.64 | 64.65 | 82.39 | 34.53 | 49.68 | 32.15 | 9.22 | 21.47 | 76.91 | 29.91 | 43.10 |

Table 3: Evaluation of zero-shot adverse weather performance across data augmentation techniques. We evaluate each data augmentation method across four different weather scenarios from the Adverse Conditions Dataset with Correspondences (ACDC) [Sakaridis et al. 2021] dataset. Each model is trained only with Cityscapes clean data. Our method, highlighted in grey, maintains the best performance across nearly all metrics for three out of four scenarios, with relative mIoU improvement up to +78.9% on fog, +44.9% on rain, +62.3% on night, and +60.0% on snow scenarios over the baseline. Degraded improvement on the Night scenario may be due to the equal weighting given to each augmentation type. For example, lowering brightness may replicate a similar effect to night time driving, and requires more frequency during training. However, equal weighting of all augmentation classes may prevent night-like augmentations from being applied during training. Fine-tuning the probability density function to account for augmentation class performance imbalances may address this discrepancy.

| Dataset | Type | Method | Clean | | | Basis Aug | | | AdvSteer [2021] | | | IN-C [2019] | | |
|-------------------|---------|--------|-----------------|-----------------|-----------------|-----------------|-----------------|-----------------|-----------------|-----------------|-----------------|-----------------|-----------------|-----------------|
| | | | aAcc \uparrow | mAcc \uparrow | mIoU \uparrow | aAcc \uparrow | mAcc \uparrow | mIoU \uparrow | aAcc \uparrow | mAcc \uparrow | mIoU \uparrow | aAcc \uparrow | mAcc \uparrow | mIoU \uparrow |
| ADE20K [2019] | General | SOTA | 77.240 | 43.010 | 33.650 | 68.156 | 34.558 | 26.229 | 37.253 | 11.150 | 7.755 | 58.146 | 23.545 | 17.561 |
| | | Ours | 77.340 | 43.000 | 33.910 | 69.234 | 35.764 | 27.317 | 39.293 | 11.403 | 8.078 | 57.971 | 23.502 | 17.624 |
| VOC2012 [2012] | General | SOTA | 81.370 | 39.990 | 30.700 | 76.131 | 34.848 | 25.448 | 71.475 | 8.763 | 6.618 | 73.116 | 17.507 | 12.909 |
| | | Ours | 80.940 | 39.690 | 30.190 | 76.410 | 34.043 | 25.297 | 70.450 | 9.040 | 6.797 | 73.150 | 16.348 | 12.148 |
| POTSDAM [[n. d.]] | Aerial | SOTA | 83.400 | 76.400 | 66.700 | 74.538 | 68.810 | 57.493 | 41.685 | 33.992 | 22.712 | 44.668 | 39.602 | 27.048 |
| | | Ours | 83.450 | 76.660 | 66.970 | 76.924 | 71.338 | 60.127 | 40.668 | 30.695 | 19.690 | 43.587 | 40.288 | 27.533 |
| LoveDA [2021] | Aerial | SOTA | 65.550 | 58.820 | 46.550 | 51.566 | 47.853 | 34.535 | 31.132 | 22.877 | 11.510 | 44.385 | 33.142 | 21.262 |
| | | Ours | 65.880 | 58.980 | 46.490 | 58.940 | 51.528 | 38.795 | 27.115 | 22.807 | 11.298 | 45.431 | 33.318 | 21.541 |
| A2I2Haze [2023] | UGV | SOTA | 98.740 | 81.500 | 71.100 | 95.684 | 70.268 | 60.546 | 66.255 | 22.018 | 15.093 | 92.397 | 45.166 | 37.589 |
| | | Ours | 98.680 | 80.370 | 70.490 | 95.952 | 70.485 | 61.965 | 79.980 | 22.037 | 17.055 | 95.276 | 46.730 | 39.873 |
| Cityscapes [2016] | Driving | SOTA | 94.910 | 77.270 | 69.860 | 83.015 | 61.137 | 52.066 | 20.332 | 13.877 | 6.685 | 63.182 | 39.839 | 31.459 |
| | | Ours | 95.100 | 79.320 | 71.840 | 88.478 | 67.400 | 58.417 | 30.020 | 16.655 | 9.300 | 63.044 | 41.299 | 32.590 |
| Synapse [2015] | Medical | SOTA | 99.000 | 73.670 | 65.120 | 90.334 | 35.833 | 28.833 | 79.152 | 18.705 | 12.913 | 83.413 | 37.630 | 30.958 |
| | | Ours | 99.150 | 79.960 | 70.410 | 88.923 | 43.111 | 34.529 | 76.308 | 22.125 | 15.912 | 82.737 | 46.105 | 37.098 |

Table 4: Performance evaluation of our method versus SOTA on synthetic corrupted scenarios, across seven datasets of varying types. We evaluate our method and SOTA on ADE20K, VOC2012, POTSDAM, LoveDA, A2I2Haze, Cityscapes, and Synapse datasets, across three synthetic corruption scenarios: individual basis augmentations, compositions of photometric augmentations produced by sensitivity analysis in Adversarial Steering [2021], and the synthetic augmentation benchmark ImageNet-C [2019]. Our method consistently achieves improved performance on synthetic corruption benchmarks while still maintaining or even improving clean evaluation accuracy. Our method works particularly well for driving and medical datasets, with a relative mIoU improvement of up to a +8% on clean evaluation and +19.8% on ImageNet-C compared to SOTA for Synapse, as well as a +2.8% relative mIoU improvement on clean evaluation and a +39.12% relative mIoU improvement on AdvSteer for Cityscapes.

augmentation techniques. In addition, our method does not require an external trained policy, unlike methods such as AutoAugment.

Metrics. We use three different metrics for evaluating the performance of a segmentation model: absolute pixel accuracy (aAcc), mean pixel accuracy (mAcc) over classes, and mean Intersection-over-Union (mIoU) over classes. All three metrics have both benefits and drawbacks. aAcc is the most intuitive, being the total number of correctly classified pixels in an image. However, aAcc is most highly influenced by class imbalances. For example, if most of an image is classified as “background”, a poorly generalized model always predicting “background” for all pixels will still achieve high

aAcc. mAcc accounts for the class imbalances by averaging pixel accuracy over all classes. That is, for each pixel in the ground truth annotation map, mAcc quantifies how many pixels per class were classified correctly. mAcc suffers from the same class imbalance example as aAcc, but to a lesser extent due to accounting for other class accuracies. Lastly, mIoU quantifies the intersection, or agreement, of predicted classes versus the ground truth class of an image. Of the three metrics, mIoU suffers the least from class imbalances, but is also the least intuitive. In all three metrics, higher values indicate better performance.

| Method | Clean | | | Basis Aug | | | AdvSteer [2021] | | | IN-C [2019] | | | ACDC [2021] | | |
|---------------|-----------------|-----------------|-----------------|-----------------|-----------------|-----------------|-----------------|-----------------|-----------------|-----------------|-----------------|-----------------|-----------------|-----------------|-----------------|
| | aAcc \uparrow | mAcc \uparrow | mIoU \uparrow | aAcc \uparrow | mAcc \uparrow | mIoU \uparrow | aAcc \uparrow | mAcc \uparrow | mIoU \uparrow | aAcc \uparrow | mAcc \uparrow | mIoU \uparrow | aAcc \uparrow | mAcc \uparrow | mIoU \uparrow |
| Baseline | 63.770 | 48.695 | 35.715 | 81.278 | 54.121 | 44.511 | 24.212 | 9.382 | 4.270 | 66.379 | 33.009 | 24.932 | 52.380 | 14.620 | 26.010 |
| Ours- $_{SA}$ | 93.950 | 77.210 | 69.670 | 83.884 | 61.860 | 52.925 | 26.523 | 15.250 | 8.467 | 63.259 | 39.028 | 31.361 | 69.850 | 27.130 | 41.030 |
| Ours- $_{g}$ | 81.185 | 52.385 | 42.410 | 82.650 | 62.004 | 49.962 | 25.138 | 11.157 | 5.308 | 63.783 | 32.053 | 23.372 | 64.810 | 24.430 | 36.810 |
| Ours- $_{p}$ | 94.840 | 77.950 | 70.210 | 87.898 | 64.524 | 55.455 | 27.388 | 15.220 | 8.435 | 60.353 | 39.779 | 31.351 | 69.470 | 27.220 | 43.450 |
| Ours | 95.100 | 79.320 | 71.840 | 88.478 | 67.400 | 58.417 | 30.020 | 16.655 | 9.300 | 63.044 | 41.299 | 32.590 | 69.330 | 26.340 | 43.790 |

Table 5: Full ablation study results comparing different variants of our method. We compare: (1) a baseline trained with no augmentations, (2) a variant of our method with uniform augmentation (Uniform), which is not informed by sensitivity analysis, (3) a variant of our method that only augments with photometric augmentations (Ours- $_{g}$), (4) a variant of our method that only uses geometric augmentations (Ours- $_{p}$), and (5) our full method combining informed probability sampling, and adaptive sensitivity analysis, and all augmentation types (Ours). Models are assessed on clean data, basis augmentations, composed perturbations from AdvSteer [2021], synthetic corruptions from ImageNet-C [2019], and real-world adverse conditions from the ACDC dataset [2021]. Our full method (Ours) consistently outperforms other variants across most metrics and scenarios, achieving the highest mIoU scores on clean data (2x), single perturbations (1.3x), combination perturbations (2.1x), and synthetic corruptions (1.3x).

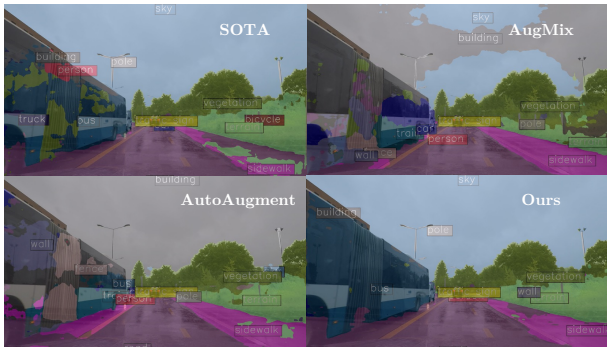


Figure 6: Qualitative comparison on rainy urban driving sample between four methods: SOTA, AugMix [Hendrycks et al. 2020], AutoAugment [Cubuk et al. 2020], and Ours. In this example, each method (SOTA, AugMix, AutoAugment, Ours) is trained on clean Cityscapes data representing sunny weather, then evaluated on adverse weather samples. Despite not having rainy data in the training set, our method is able to segment the driving noticeably clearer than other methods. In particular, other methods consistently struggle to segment the bus (blue, left) confidently.

5.1 Comparison to Other Techniques

We compare our results to six methods: a baseline model where no augmentation is performed, AugMix [Hendrycks et al. 2020], AutoAugment [Cubuk et al. 2019], RandAugment [Cubuk et al. 2020], TrivialAugment [Muller and Hutter 2021], and a trained state-of-the-art (SOTA) model for the experiment configuration. Since popular augmentation techniques such as AugMix and AutoAugment are typically not applied to segmentation models, we define the SOTA model as the best-performing training configuration made available by maintainers. These configurations may have a variety of different augmentations applied depending on the training dataset; we generically refer to these models as ‘‘SOTA’’, simply because they are the best available segmentation model.

We show a comparison across augmentation techniques on overall model performance on Cityscapes for two architectures, PSPNet [Zhao et al. 2017] and Segformer [Xie et al. 2021], in Table 1.

On the PSPNet architecture, our method achieves 101.1% improvement in mIoU compared to the baseline, while the next best method achieves 95.6% improvement. Similarly, we also compare results on SegFormer, which is a modern transformer-based architecture known for its robustness. However, in contrast to our method and other data augmentation techniques, the robustness offered by SegFormer comes from its architecture design. We emphasize that our method can be used in conjunction with SegFormer to offer even better results. On SegFormer, we achieve 57.8% mIoU improvement over the baseline while the current SOTA method achieves 57.7% improvement. Expectedly, the effects of our method diminish relative to baselines as the model becomes more inherently robust.

5.2 Evaluation on Real-World Adverse Samples

To evaluate the robustness of our model in visual and graphics applications, we test on real-world adverse samples. While real-world adverse samples in most datasets are difficult to obtain, there are numerous real-world datasets for driving representing different cities and adverse weather scenarios.

We evaluate our Cityscapes models on two real-world datasets: the Adverse Conditions Dataset with Correspondences (ACDC) [Sakaridis et al. 2021] dataset which represents adverse weather, and the India Driving Dataset (IDD) [Varma et al. 2019] which represents an alternative, more heterogeneous domain. IDD represents an alternative, but similar, domain in which visual appearances of vehicles, traffic, and scenery may slightly change, in addition to co-occurrences of classes. We emphasize that, for this experiment, models are only trained on Cityscapes, and evaluation on such scenarios can be considered zero-shot generalization.

Overall performance on both ACDC and IDD datasets across multiple methods can be found in Table 2. On real-world dataset evaluation for zero-shot weather and domain gap scenarios, our method shows clear improvements over the next best performing model across almost all metrics. We include a qualitative visualization of our model versus several other methods in Figure 6, which shows inference on a rainy weather sample. While our method is outperformed by SOTA on aAcc for the IDD dataset, we note that our method achieves higher scores for mAcc and mIoU, which may be indicative of class imbalances within the dataset.

Furthermore, we break down the performance on the ACDC dataset by weather type in Table 3. In total, the ACDC dataset

has four different weather scenarios: Fog, Rain, Night, and Snow. In three out of four weather categories, our method outperforms other methods, with the exception of Night scenarios. While our model still achieves better performance than SOTA and the baseline, the degraded improvement compared to AutoAugment may be attributed to the equal weighting of augmentation classes in our sampling routine. For example, the model may be particularly brittle to augmentations simulating lower brightness, but its weight is limited to, at most, a probability of $\frac{1}{25}$. In techniques such as AutoAugment, an entirely different policy is trained offline to guide learning; thus, such limitations on sampling may not exist. In context of our method, we may be able to achieve higher improvements on Night driving by fine tuning the augmentation sampling strategy to favor lower-lighting augmentations.

5.3 Evaluation on Diverse Datasets

The results in previous experiments show the efficacy of our method in context of driving domains. In this experiment, we demonstrate that our method also shows improvements across several datasets and visual computing domains compared to SOTA.

We evaluate our method on seven semantic segmentation datasets: ADE20K [Zhou et al. 2019], VOC2012 [Everingham et al. 2012], POTSDAM [for Photogrammetry and Sensing [n. d.]], LoveDA [Wang et al. 2021], Cityscapes [Cordts et al. 2016], Synapse [Landman et al. 2015], and A2I2Haze [Narayanan et al. 2023]. POTSDAM and LoveDA are both remote sensing datasets taken from aerial views, with classes focusing on classification of buildings, roads, trees, etc. POTSDAM describes aerial imagery in Potsdam, Germany, whereas LoveDA contains scenery from Wuhan, China. Cityscapes is a popular benchmark dataset for segmentation in urban traffic scenes, with annotations describing classes such as terrain, human, and vehicle types. ADE20K and VOC2012 are generic datasets describing everyday life and objects, with both indoor and outdoor scenes. Synapse is a medical imaging dataset of clinically-acquired CT scans. In our experiments, we use abdomen data and classify organs. A2I2Haze is a dataset representing outdoor clear and hazy data collected from unmanned robots for scene understanding. We use the UGV, or Unmanned Ground Vehicle data in our experiments, which is similar to autonomous driving datasets except in more heterogeneous outdoor environments.

In Table 4, we show mIoU performance of our method versus the next-best augmentation technique, the SOTA baseline. We evaluate on clean data and three different synthetic scenarios: individual transformations from the basis augmentations at uniform parameter intervals, the combined perturbation benchmark from [Shen et al. 2021], and ImageNet-C [Hendrycks and Dietterich 2019] corruptions. ***In nearly all dataset settings, our model achieves improved scores, particularly in the robotics and medical domains.*** Models trained on A2I2Haze and Cityscapes see improved robustness in all three corrupted scenarios, while Cityscapes actually sees a small boost in clean accuracy. In previous works using sensitivity analysis, augmentations which typically increase robustness also degrade clean accuracy. In our case, clean accuracy is either improved or maintained. Qualitative results on synapse can be observed in Figure 2. In this figure, we show two common synthetic perturbations naturally occurring in medical datasets: jpeg

compression and motion blur. While medical domains often have much more standardized data than others, such applications are not immune to human error in the data logging process.

Across dataset categories, we observe that the least improvement gained is in the General category, where the dataset consists of everyday scenes or items. In these datasets, the total number of classes is much higher than those of datasets with more specific domains, and total dataset size is typically larger. Data augmentation excels particularly in domains with limited samples; with larger datasets, the effects of data augmentation may be less pronounced, since there may be diverse representations of each class from different domains, taken with different cameras, in different lighting, etc. In other words, the corruptions may already be inherently captured in the training data.

5.4 Ablation Study.

To examine the effects of each component in our method, we conduct an ablation study. In Table 5, we show several variants of our method and their performance on three synthetic scenarios, which are similar to Table 4, and one real-world scenario (ACDC). We study (1) the effect of sensitivity analysis on overall performance (Ours_{~SA}), (2) the effect of geometric augmentations on overall performance (Ours_{~g}), and (3) the effect of photometric augmentations (Ours_{~p}) on overall performance. We choose to delineate photometric and geometric augmentations specifically to examine their effects on robustness while sensitivity analysis prioritizes augmentations with weaker performance. Previous work has shown that geometric augmentations play a large role in model performance [Alomar et al. 2023]; we corroborate this even in interaction with sensitivity analysis.

The model trained without geometric augmentations has a severe degradation in model performance, even if worse-performing photometric augmentations are prioritized during learning using sensitivity analysis. This may suggest that photometric robustness and geometric robustness play a distinct role for segmentation specifically; a model generalizing to differences in lighting may still have high geometric variance. Since photometric augmentations still preserve local differences in pixel values to some degree, ablation study results may suggest that segmentations models lean heavily on local pixel differences rather than innately identifying objects as a whole.

Overall, we find all components of our method to contribute towards general improvements in robustness across several domains, where the ***most significant boost in performance stems from the involvement of geometric augmentations and our sensitivity analysis augmentation scheme.***

6 CONCLUSION

In this paper, we present a method for sensitivity-informed augmented training for semantic segmentation. Our method combines the information granularity of sensitivity analysis-based methods and the scalability of data augmentation methods, which run on-the-fly during training. In our results, we show that our method achieves higher clean accuracy results on different backbones and numerous datasets. Additionally, evaluation on real world datasets

show clear improvements over current SOTA methods for augmentation. The ablation study then shows that boosts in performance stem mostly from geometric transformations in addition to sensitivity analysis. Future work may explore more sophisticated policies for augmentation sampling strategies; in our method, we simply weight all augmentation classes equally and weight augmentation magnitudes by the results of the sensitivity analysis. Overall, we find this work to be broadly beneficial to any visual computing and computer graphics application, where segmentation and scene understanding is an integral part of the pipeline.

REFERENCES

- Khaled Alomar, Halil Ibrahim Aysel, and Xiaohao Cai. 2023. Data Augmentation in Classification and Segmentation: A Survey and New Strategies. *J Imaging* 9, 2 (Feb. 2023).
- M. Bińkowski, D. J. Sutherland, M. Arbel, and A. Gretton. 2018. Demystifying MMD GANs. *arXiv preprint arXiv:1801.01401* (2018).
- MMSegmentation Contributors. 2020. MMSegmentation: OpenMMLab Semantic Segmentation Toolbox and Benchmark. <https://github.com/open-mmlab/mms Segmentation>.
- Marius Cordts, Mohamed Omran, Sebastian Ramos, Timo Rehfeld, Markus Enzweiler, Rodrigo Benenson, Uwe Franke, Stefan Roth, and Bernt Schiele. 2016. The Cityscapes Dataset for Semantic Urban Scene Understanding. In *Proc. of the IEEE Conference on Computer Vision and Pattern Recognition (CVPR)*.
- Ekin D. Cubuk, Barret Zoph, Dandelion Mané, Vijay Vasudevan, and Quoc V. Le. 2019. AutoAugment: Learning Augmentation Strategies From Data. In *2019 IEEE/CVF Conference on Computer Vision and Pattern Recognition (CVPR)*. 113–123. <https://doi.org/10.1109/CVPR.2019.00020>
- Ekin Dogus Cubuk, Barret Zoph, Jon Shlens, and Quoc Le. 2020. RandAugment: Practical Automated Data Augmentation with a Reduced Search Space. In *Advances in Neural Information Processing Systems*. 18613–18624.
- Yinpeng Dong, Qi-An Fu, Xiao Yang, Tianyu Pang, Hang Su, Zihao Xiao, and Jun Zhu. 2020. Benchmarking Adversarial Robustness on Image Classification. In *Proceedings of the IEEE/CVF Conference on Computer Vision and Pattern Recognition (CVPR)*.
- M. Everingham, L. Van Gool, C. K. I. Williams, J. Winn, and A. Zisserman. 2012. The PASCAL Visual Object Classes Challenge 2012 (VOC2012) Results. <http://www.pascal-network.org/challenges/VOC/voc2012/workshop/index.html>.
- International Society for Photogrammetry and Remote Sensing. [n.d.]. POTSDAM: 2D Semantic Labeling Contest. <https://www.isprs.org/education/benchmarks/UrbanSemLab/2d-sem-label-potsdam.aspx>.
- Robert Geirhos, Patricia Rubisch, Claudio Michaelis, Matthias Bethge, Felix A. Wichmann, and Wieland Brendel. 2019. ImageNet-trained CNNs are biased towards texture; increasing shape bias improves accuracy and robustness. In *International Conference on Learning Representations*. <https://openreview.net/forum?id=Bygh9j09KX>
- Dan Hendrycks, Steven Basart, Norman Mu, Saurav Kadavath, Frank Wang, Evan Dorundo, Rahul Desai, Tyler Zhu, Samyak Parajuli, Mike Guo, Dawn Song, Jacob Steinhardt, and Justin Gilmer. 2021. The Many Faces of Robustness: A Critical Analysis of Out-of-Distribution Generalization. In *Proceedings of the IEEE/CVF International Conference on Computer Vision (ICCV)*. 8340–8349.
- Dan Hendrycks and Thomas Dietterich. 2019. Benchmarking Neural Network Robustness to Common Corruptions and Perturbations. *Proceedings of the International Conference on Learning Representations* (2019).
- Dan Hendrycks and Kevin Gimpel. 2017. A Baseline for Detecting Misclassified and Out-of-Distribution Examples in Neural Networks. In *International Conference on Learning Representations*. <https://openreview.net/forum?id=Hkg4TI9xl>
- Dan Hendrycks, Norman Mu, Ekin Dogus Cubuk, Barret Zoph, Justin Gilmer, and Balaji Lakshminarayanan. 2020. AugMix: A Simple Data Processing Method to Improve Robustness and Uncertainty. In *International Conference on Learning Representations*.
- Christopher Kamann and Carsten Rother. 2020. Benchmarking the Robustness of Semantic Segmentation Models. In *Proceedings of the IEEE/CVF Conference on Computer Vision and Pattern Recognition (CVPR)*.
- Bennett Landman, Zhoubing Xu, Juan Eugenio Iglesias, Martin Styner, Thomas Robin Langerak, and Arno Klein. 2015. Multi-Atlas Labeling Beyond the Cranial Vault - Workshop and Challenge. <https://www.synapse.org/#!/Synapse:syn3193805/wiki/89480>.
- Eric Mintun, Alexander Kirillov, and Saining Xie. 2021. On Interaction Between Augmentations and Corruptions in Natural Corruption Robustness. In *Advances in Neural Information Processing Systems*, M. Ranzato, A. Beygelzimer, Y. Dauphin, P.S. Liang, and J. Wortman Vaughan (Eds.), Vol. 34. Curran Associates, Inc., 3571–3583. https://proceedings.neurips.cc/paper_files/paper/2021/file/1d49780520898fe37f0cd6b41c5311bf-Paper.pdf
- Samuel G. Muller and Frank Hutter. 2021. TrivialAugment: Tuning-free Yet State-of-the-Art Data Augmentation. In *IEEE/CVF International Conference on Computer Vision (ICCV)*. 754–762.
- Priya Narayanan, Xin Hu, Zhenyu Wu, Matthew D. Thielke, John G. Rogers, Andre V. Harrison, John A. D’Agostino, James D. Brown, Long P. Quang, James R. Uplinger, Heesung Kwon, and Zhangyang Wang. 2023. A Multi-Purpose Realistic Haze Benchmark With Quantifiable Haze Levels and Ground Truth. *IEEE Transactions on Image Processing* 32 (2023), 3481–3492. <https://doi.org/10.1109/TIP.2023.3245994>
- Viktor Olsson, Wilhelm Tranheden, Juliano Pinto, and Lennart Svensson. 2021. ClassMix: Segmentation-Based Data Augmentation for Semi-Supervised Learning. In *Proceedings of the IEEE/CVF Winter Conference on Applications of Computer Vision (WACV)*. 1369–1378.
- Evgenia Ruskak, Lukas Schott, Roland S. Zimmermann, Julian Bitterwolf, Oliver Bringmann, Matthias Bethge, and Wieland Brendel. 2020. A Simple Way to Make Neural Networks Robust Against Diverse Image Corruptions. In *Computer Vision – ECCV 2020*, Andrea Vedaldi, Horst Bischof, Thomas Brox, and Jan-Michael Frahm (Eds.). Springer International Publishing, Cham, 53–69.
- Tommy Saikia, Cordelia Schmid, and Thomas Brox. 2021. Improving Robustness Against Common Corruptions With Frequency Biased Models. In *Proceedings of the IEEE/CVF International Conference on Computer Vision (ICCV)*. 10211–10220.
- Christos Sakaridis, Dengxin Dai, and Luc Van Gool. 2021. ACDC: The Adverse Conditions Dataset with Correspondences for Semantic Driving Scene Understanding. In *Proceedings of the IEEE/CVF International Conference on Computer Vision (ICCV)*.
- Steffen Schneider, Evgenia Ruskak, Luisa Eck, Oliver Bringmann, Wieland Brendel, and Matthias Bethge. 2020. Improving robustness against common corruptions by covariate shift adaptation. In *Advances in Neural Information Processing Systems*, H. Larochelle, M. Ranzato, R. Hadsell, M.F. Balcan, and H. Lin (Eds.), Vol. 33. Curran Associates, Inc., 11539–11551. https://proceedings.neurips.cc/paper_files/paper/2020/file/85690f81aad1749175c187784af9e9e-Paper.pdf
- Yu Shen, Laura Zheng, Manli Shu, Weizi Li, Tom Goldstein, and Ming Lin. 2021. Gradient-Free Adversarial Training Against Image Corruption for Learning-based Steering. In *Advances in Neural Information Processing Systems*, M. Ranzato, A. Beygelzimer, Y. Dauphin, P.S. Liang, and J. Wortman Vaughan (Eds.), Vol. 34. Curran Associates, Inc., 26250–26263. https://proceedings.neurips.cc/paper_files/paper/2021/file/dce8af15f064d1accb98887a21029b08-Paper.pdf
- Girish Varma, Anbumani Subramanian, Anoop Nambodiri, Manmohan Chandraker, and C.V. Jawahar. 2019. IDD: A Dataset for Exploring Problems of Autonomous Navigation in Unconstrained Environments. In *2019 IEEE Winter Conference on Applications of Computer Vision (WACV)*. 1743–1751. <https://doi.org/10.1109/WACV.2019.00190>
- Junjue Wang, Zhuo Zheng, Ailong Ma, Xiaoyan Lu, and Yanfei Zhong. 2021. LoveDA: A Remote Sensing Land-Cover Dataset for Domain Adaptive Semantic Segmentation. In *Proceedings of the Neural Information Processing Systems Track on Datasets and Benchmarks*, J. Vanschoren and S. Yeung (Eds.), Vol. 1. Curran Associates, Inc. https://datasets-benchmarks-proceedings.neurips.cc/paper_files/paper/2021/file/4e732ced3463d06de0ca9a15b6153677-Paper-round2.pdf
- Enze Xie, Wenhai Wang, Zhiding Yu, Anima Anandkumar, Jose M. Alvarez, and Ping Luo. 2021. SegFormer: Simple and Efficient Design for Semantic Segmentation with Transformers. In *Advances in Neural Information Processing Systems*, M. Ranzato, A. Beygelzimer, Y. Dauphin, P.S. Liang, and J. Wortman Vaughan (Eds.), Vol. 34. Curran Associates, Inc., 12077–12090. https://proceedings.neurips.cc/paper_files/paper/2021/file/64f1f27bf1b4ec22924f0ac6550c235-Paper.pdf
- Chenyu Yi, SIYUAN YANG, HaoLiang Li, Yap peng Tan, and Alex Kot. 2021. Benchmarking the Robustness of Spatial-Temporal Models Against Corruptions. In *Thirty-fifth Conference on Neural Information Processing Systems Datasets and Benchmarks Track (Round 2)*. <https://openreview.net/forum?id=MQIMlr3Hv5>
- Sangdoon Yun, Dongyoon Han, Seong Joon Oh, Sanghyuk Chun, Junsuk Choe, and Youngjoon Yoo. 2019. CutMix: Regularization Strategy to Train Strong Classifiers with Localizable Features. In *International Conference on Computer Vision (ICCV)*.
- Xinru Zhang, Chenghao Liu, Ni Ou, Xiangzhu Zeng, Zhizheng Zhuo, Yunyun Duan, Xiaoliang Xiong, Yizhou Yu, Zhiwen Liu, Yaou Liu, and Chuyang Ye. 2023. CarveMix: A simple data augmentation method for brain lesion segmentation. *NeuroImage* 271 (2023), 120041. <https://doi.org/10.1016/j.neuroimage.2023.120041>
- Amy Zhao, Guha Balakrishnan, Fredo Durand, John V. Guttag, and Adrian V. Dalca. 2019. Data Augmentation Using Learned Transformations for One-Shot Medical Image Segmentation. In *Proceedings of the IEEE/CVF Conference on Computer Vision and Pattern Recognition (CVPR)*.
- Hengshuang Zhao, Jianping Shi, Xiaojuan Qi, Xiaogang Wang, and Jiaya Jia. 2017. Pyramid Scene Parsing Network. In *IEEE Conference on Computer Vision and Pattern Recognition (CVPR)*.
- Yu Zheng, Zhi Zhang, Shen Yan, and Mi Zhang. 2022. Deep AutoAugmentation. In *ICLR*.
- Bolei Zhou, Hang Zhao, Xavier Puig, Tete Xiao, Sanja Fidler, Adela Barriuso, and Antonio Torralba. 2019. Semantic understanding of scenes through the ade20k dataset. *International Journal of Computer Vision* 127, 3 (2019), 302–321.

A ADDITIONAL PHOTOMETRIC AUGMENTATIONS

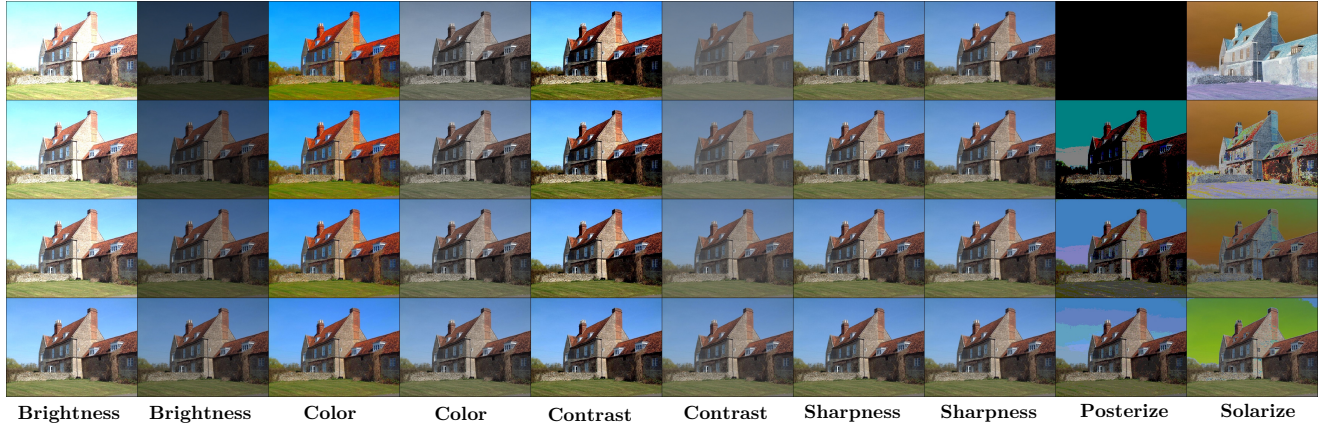


Figure 7: Additional augmentation types used in sensitivity analysis, which are used in other methods such as AutoAugment. While these photometric transformations are used in other methods, the transformations also overlap with the photometric transformations shown in Figure 4, namely HSV perturbations. However, we still conduct sensitivity analysis evaluation on these transformations for completion.

B FAST SENSITIVITY ANALYSIS ALGORITHM

Algorithm 1: Fast Sensitivity Analysis

Data: Number of levels L , Uncertainty threshold ϵ

Result: Perturbation Levels $\{\alpha_1, \dots, \alpha_{L-1}\}$

```

1  $g(\alpha) \leftarrow$  Equation 8;
2 points  $\leftarrow \{(0, 0), (\alpha_L, 2)\}$ ;
3 loop
4    $\hat{c} \leftarrow$  PCHIP(points);
5   for  $i \leftarrow 1 \dots L - 1$  do
6      $\alpha_i \leftarrow$  Estimate( $\hat{c}$ ,  $2i/L$ );
7      $(y_l, y_u) \leftarrow$  Estimate upper and lower y-values of  $\hat{c}$  at  $x = \alpha_i$ ;
8      $\hat{c}_l \leftarrow$  PCHIP(points.insert( $y_l$ ));
9      $\hat{c}_u \leftarrow$  PCHIP(points.insert( $y_u$ ));
10     $\alpha_{i_l} \leftarrow$  Estimate( $\hat{c}$ ,  $y_l$ );
11     $\alpha_{i_u} \leftarrow$  Estimate( $\hat{c}$ ,  $y_u$ );
12     $\epsilon_i \leftarrow (\alpha_{i_u} - \alpha_{i_l})/2$ ;
13  end
14   $\alpha^*, \epsilon^* \leftarrow$  Choose level with max  $\epsilon_i$ ;
15  if  $\epsilon^* < \epsilon$  then Break loop;
16  points.insert( $(\alpha^*, g(\alpha^*))$ );
17 end;
```

C FAST SENSITIVITY ANALYSIS ILLUSTRATION

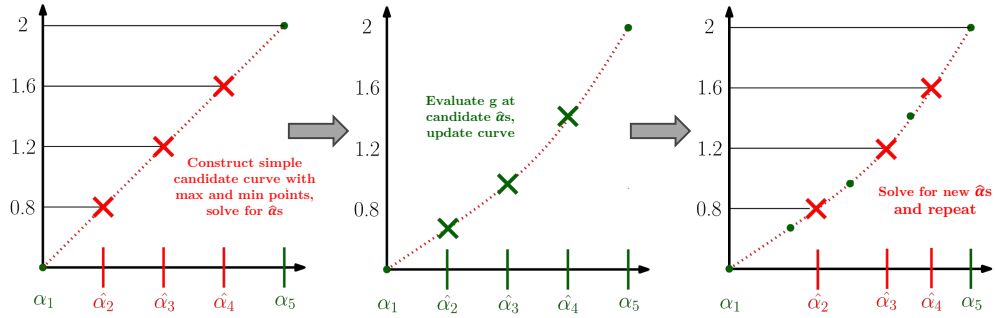


Figure 8: Illustration of fast sensitivity analysis. Each iteration of the fast sensitivity can be intuitively visualized. Since we can assume general monotonicity of the curve, we first initialize a candidate curve (a line in the first iteration). We solve for the candidate perturbation levels $\hat{\alpha}$ based on the solution in Equation 9. In the next step (middle), we evaluate the candidate level with the greatest uncertainty and adjust the candidate curve, the dotted red line, since the evaluated levels are guaranteed to be true points along the function g from Equation 8. In the next step (right), we use the new curve and solve for new candidate levels, repeating the process in the previous two steps until the maximum uncertainty of any candidate level values falls below a certain threshold.

D SENSITIVITY ANALYSIS COMPUTED CURVE COMPARISON

| Perturb | Method | p_1 | p_2 | p_3 | p_4 |
|------------------|----------|-------|-------|-------|-------|
| R_{\uparrow} | Baseline | 0.100 | 0.300 | 0.500 | 0.700 |
| | Adaptive | 0.149 | 0.253 | 0.399 | 0.604 |
| G_{\uparrow} | Baseline | 0.100 | 0.200 | 0.400 | 0.600 |
| | Adaptive | 0.103 | 0.204 | 0.395 | 0.619 |
| B_{\uparrow} | Baseline | 0.200 | 0.300 | 0.500 | 0.700 |
| | Adaptive | 0.146 | 0.328 | 0.551 | 0.788 |
| R_{\downarrow} | Baseline | 0.200 | 0.400 | 0.600 | 0.800 |
| | Adaptive | 0.225 | 0.503 | 0.625 | 0.803 |
| G_{\downarrow} | Baseline | 0.200 | 0.400 | 0.600 | 0.800 |
| | Adaptive | 0.256 | 0.447 | 0.607 | 0.812 |
| B_{\downarrow} | Baseline | 0.200 | 0.500 | 0.700 | 0.800 |
| | Adaptive | 0.231 | 0.450 | 0.594 | 0.730 |
| H_{\uparrow} | Baseline | 0.100 | 0.300 | 0.400 | 0.900 |
| | Adaptive | 0.268 | 0.406 | 0.508 | 0.809 |
| S_{\uparrow} | Baseline | 0.200 | 0.500 | 0.600 | 0.800 |
| | Adaptive | 0.243 | 0.439 | 0.589 | 0.744 |
| V_{\uparrow} | Baseline | 0.200 | 0.400 | 0.600 | 0.700 |
| | Adaptive | 0.193 | 0.360 | 0.517 | 0.680 |
| H_{\downarrow} | Baseline | 0.200 | 0.400 | 0.500 | 0.600 |
| | Adaptive | 0.279 | 0.433 | 0.548 | 0.699 |
| S_{\downarrow} | Baseline | 0.200 | 0.400 | 0.600 | 0.900 |
| | Adaptive | 0.199 | 0.344 | 0.562 | 0.847 |
| V_{\downarrow} | Baseline | 0.200 | 0.400 | 0.600 | 0.800 |
| | Adaptive | 0.197 | 0.397 | 0.594 | 0.797 |
| <i>blur</i> | Baseline | 9 | 19 | 25 | 35 |
| | Adaptive | 9 | 17 | 23 | 31 |
| <i>noise</i> | Baseline | 10 | 15 | 20 | 30 |
| | Adaptive | 6.4 | 12.4 | 17.7 | 26.9 |

Table 6: Comparison of computed perturbation levels using a baseline [Shen et al. 2021] sensitivity analysis method versus our adaptive method. p_5 is 1 for all RGB/HSV channels, 49 for blur, and 50 for noise. In previous work, each perturbation level is chosen from a certain number of sampled, discretized values. Additionally, these perturbed datasets are generated offline in an additional step before training. Our fast sensitivity analysis enables sensitivity analysis to be performed on the fly during training, and offers much more dynamic, accurate, and descriptive sensitivity curves.

E KID VS. FID RELATIVE ERROR COMPARISON WITH SCALING SAMPLE SIZES

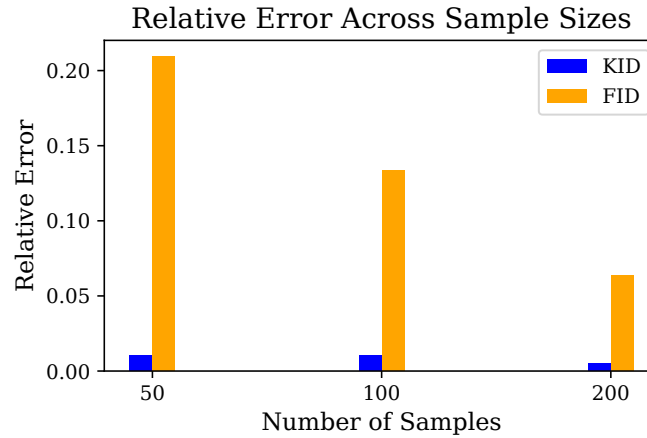


Figure 9: Relative error of KID and FID over several sample sizes. We plot the relative error of computed KID and FID values over several sample sizes, with the reference value being the computed value for each at 500 samples. From this, we can see that FID is significantly biased toward the number of samples used for evaluation. We can reduce the evaluation of KID values in sensitivity analysis by a notable fraction due to this property.

F TRAIN-TIME EVALUATION ON PERTURBED DATASETS

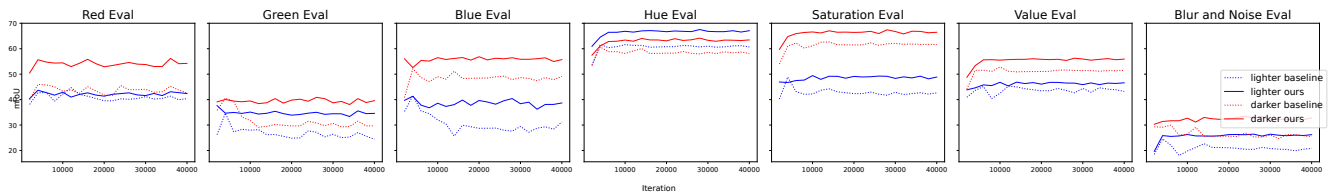


Figure 10: Evaluation on perturbed test datasets over training iterations. We show the evaluation on each perturbed dataset during training of our model and the baseline for VOC2012 dataset.

G ADAPTIVE SENSITIVITY ANALYSIS WITH DIFFERENT NUMBER OF LEVELS

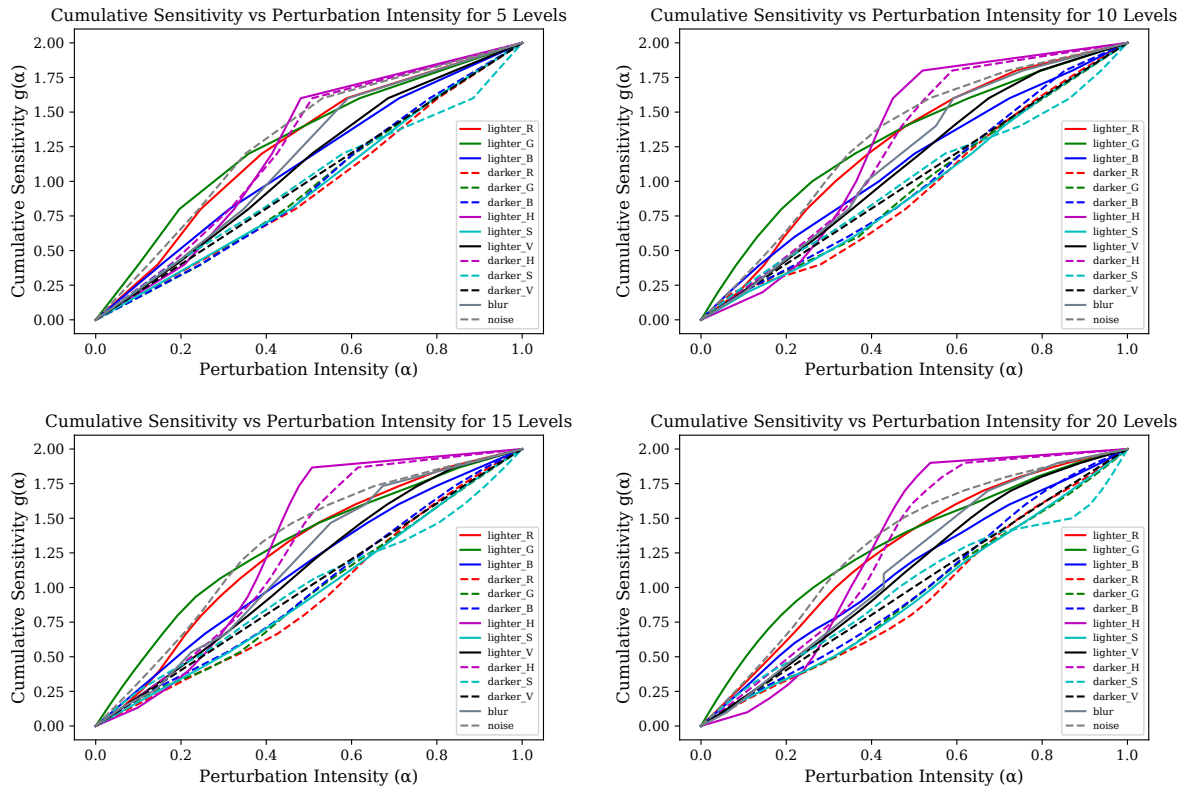


Figure 11: Visualization of cumulative sensitivity curve with varying number of levels L . We visualize the cumulative sensitivity curve in Figure 3 when computing for 5, 10, 15, and 20 levels. We find that even when we increase the number of levels, the curves remain *approximately* the same. Thus, we use 5 levels in our implementation to reduce compute for the sensitivity analysis step.

H HOW SENSITIVITY ANALYSIS CURVE CHANGES OVER TRAINING

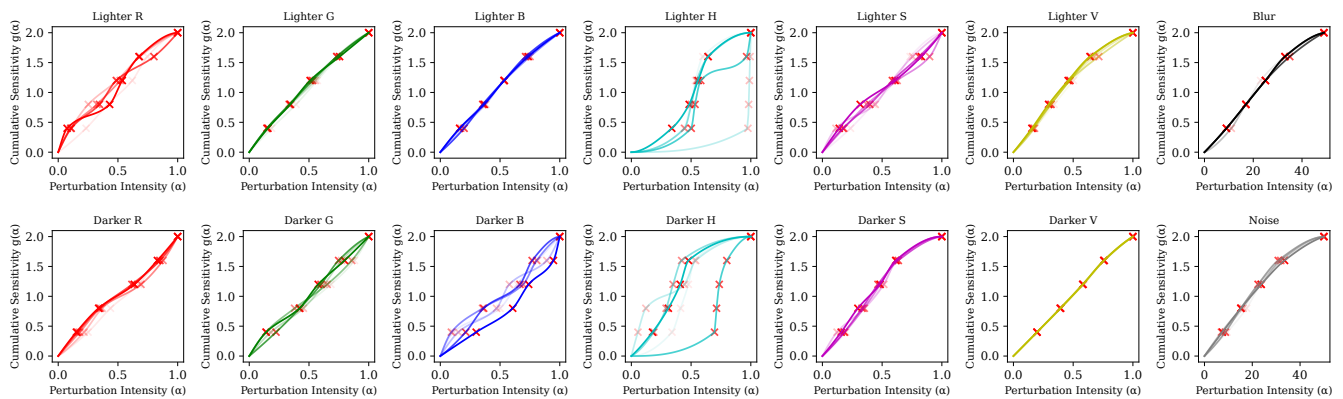


Figure 12: Cumulative sensitivity curves throughout training. We visualize how the estimated cumulative sensitivity curve changes during augmented training. In this plot, the most recent curve is opaque, while others are decrease in opacity in order of recency.

Received 20 February 2007; revised 12 March 2009; accepted 5 June 2009